Advances in Chemical Physics
Stuart A. Rice and Aaron R. Dinner, Series Editors

Advances in Chemical Physics

Volume 156

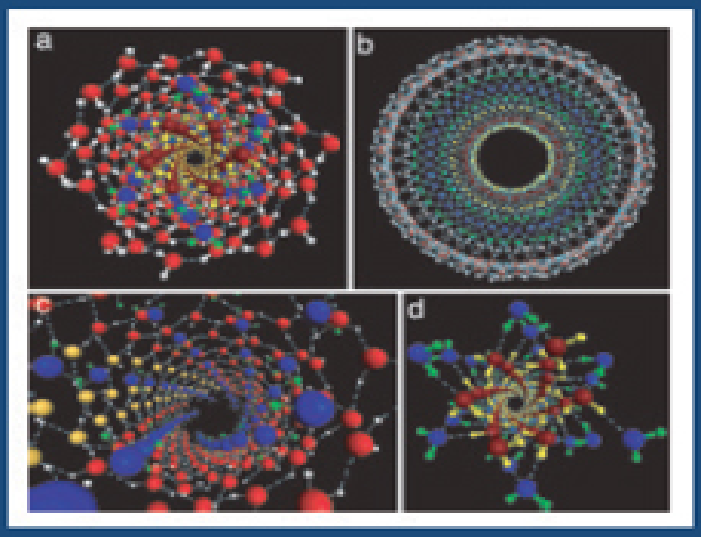

Edited by

Stuart A. Rice

Aaron R. Dinner

WILEY

EDITORIAL BOARD

TODD J. MARTINEZ
Department of Chemistry, Photon Science, Stanford University, Stanford, California USA

SHAUL MUKAMEL
Department of Chemistry, School of Physical Sciences, University of California, Irvine, California USA

JOSE N. ONUCHIC
Department of Physics, Center for Theoretical Biological Physics, Rice University, Houston, Texas USA

STEPHEN QUAKE
Department of Bioengineering, Stanford University, Palo Alto, California USA

MARK RATNER
Department of Chemistry, Northwestern University, Evanston, Illinois USA

DAVID REICHMAN
Department of Chemistry, Columbia University, New York City, New York USA

GEORGE SCHATZ
Department of Chemistry, Northwestern University, Evanston, Illinois USA

STEVEN J. SIBENER
Department of Chemistry, James Franck Institute, University of Chicago, Chicago, Illinois USA

ANDREI TOKMAKOFF
Department of Chemistry, James Franck Institute, University of Chicago, Chicago, Illinois USA

DONALD G. TRUHLAR
Department of Chemistry, University of Minnesota, Minneapolis, Minnesota USA

JOHN C. TULLY
Department of Chemistry, Yale University, New Haven, Connecticut, USA

ADVANCES IN CHEMICAL PHYSICS

VOLUME 156

Edited BY

STUART A. RICE
Department of Chemistry and The James Franck Institute,
The University of Chicago, Chicago, Illinois

AARON R. DINNER
Department of Chemistry and The James Franck Institute,
The University of Chicago, Chicago, Illinois

WILEY

Published by John Wiley & Sons, Inc., Hoboken, New Jersey.
Published simultaneously in Canada.

Library of Congress Catalog Number: 58-9935

ISBN: 978-1-118-94969-6

CONTRIBUTORS TO VOLUME 156

ANASTASSIA N. ALEXANDROVA
Department of Chemistry and Biochemistry, University of California, Los Angeles, CA, 90095-1569, USA

LOUIS-S. BOUCHARD
California NanoSystems Institute, Los Angeles, CA, 90095, USA

DECLAN J. BYRNE
School of Physics, University College Dublin, Belfield, Dublin 4, Ireland

WILLIAM T. COFFEY
Department of Electronic and Electrical Engineering, Trinity College, Dublin 2, Ireland

MARJOLEIN DIJKSTRA
Soft Condensed Matter group, Debye Institute for Nanomaterials Science, Utrecht University, Princetonplein 5, 3584 CC Utrecht, The Netherlands

WILLIAM J. DOWLING
Department of Electronic and Electrical Engineering, Trinity College, Dublin 2, Ireland

M. HAYASHI
Condensed Matter Center, National Taiwan University, Taipei, Taiwan

YURI P. KALMYKOV
Laboratoire de Mathèmatiques et Physique, Universitè de Perpignan Via Domitia, 54, Avenue Paul Alduy, F-66860 Perpignan, France

C.K. LIN
Condensed Matter Center, National Taiwan University, Taipei, Taiwan

S.H. LIN
Department of Applied Chemistry, National Chiao-Tung University, Hsinchu, Taiwan

G. ALI MANSOORI
Department of Bioengineering, University of Illinois at Chicago, Chicago, IL 60607-7052, USA

Y.L. NIU
The State Key Laboratory of Molecular Reaction Dynamics, Institute of Chemistry, Chinese Academy of Sciences, Beijing, China

RANKO RICHERT
Department of Chemistry and Biochemistry, Arizona State University, Tempe, AZ, 85287-1604, USA

STUART A. RICE
Department of Chemistry and the James Franck Institute, The University of Chicago, Chicago, IL 60637, USA

ASAF SHIMSHOVITZ
Department of Chemical Physics, Weizmann Institute of Science, Rehovot, 76100 Israel

NORIO TAKEMOTO
Department of Chemical Physics, Weizmann Institute of Science, Rehovot, 76100 Israel

DAVID J. TANNOR
Department of Chemical Physics, Weizmann Institute of Science, Rehovot, 76100 Israel

SERGUEY V. TITOV
Kotel'nikov Institute of Radio Engineering and Electronics of the Russian Academy of Sciences, Vvedenskii Square 1, Fryazino, Moscow Region, 141190, Russian Federation

L. YANG

Institute of Theoretical and Simulation Chemistry,
Academy of Fundamental and Interdisciplinary Science,
Harbin Institute of Technology, Harbin, China

C.Y. ZHU

Department of Applied Chemistry, National Chiao-Tung
University, Hsinchu, Taiwan

PREFACE TO THE SERIES

Advances in science often involve initial development of individual specialized fields of study within traditional disciplines followed by broadening and overlap, or even merging, of those specialized fields, leading to a blurring of the lines between traditional disciplines. The pace of that blurring has accelerated in the last few decades, and much of the important and exciting research carried out today seeks to synthesize elements from different fields of knowledge. Examples of such research areas include biophysics and studies of nanostructured materials. As the study of the forces that govern the structure and dynamics of molecular systems, chemical physics encompasses these and many other emerging research directions. Unfortunately, the flood of scientific literature has been accompanied by losses in the shared vocabulary and approaches of the traditional disciplines, and there is much pressure from scientific journals to be ever more concise in the descriptions of studies, to the point that much valuable experience, if recorded at all, is hidden in supplements and dissipated with time. These trends in science and publishing make this series, *Advances in Chemical Physics*, a much needed resource.

The *Advances in Chemical Physics* is devoted to helping the reader obtain general information about a wide variety of topics in chemical physics, a field that we interpret very broadly. Our intent is to have experts present comprehensive analyses of subjects of interest and to encourage the expression of individual points of view. We hope that this approach to the presentation of an overview of a subject will both stimulate new research and serve as a personalized learning text for beginners in a field.

STUART A. RICE
AARON R. DINNER

CONTENTS

List of Tables

List of Illustrations

cell of area h. For a color version of this figure, see the color plate section.

Figure 2 Classical phase space contours for (a) harmonic oscillator Hamiltonian, (b) Coulomb Hamiltonian.

Figure 3 (a) A schematic diagram of the development of the von Neumann/Gabor method in the quantum mechanics and signal processing communities. The development proceeded largely independently. (b) Quotes from the quantum mechanics and signal processing literatures indicating that the von Neumann/Gabor basis on a truncated lattice does not converge.

Figure 4 Illustration of the Dirichlet or periodic sinc functions. These functions are the underlying basis of the fast Fourier transform (discrete Fourier transform with periodic boundary conditions). They go to 1 at one of the Fourier grid points and to 0 at all the other Fourier grid points. The various members of the basis are orthonormal. For a color version of this figure, see the color plate section.

Figure 5 (a) $N = 9$ coordinate grid points and $N = 9$ Gabor unit cells cover the same area in phase space, $S = 2\pi N$. Superimposed is a typical Gabor function. Note that its boundary conditions are not appropriate for the rectangular area. (b) The periodic Gabor (pg) basis is a complete set for the truncated space. The pg basis functions are, loosely speaking, periodic and band-limited Gaussians whose centers are located at the center of each unit cell.

Figure 6 Magnitude of S (a) and S^{-1} (b) matrices on a logarithmic scale. For a color version of this figure, see the color plate section.

Figure 7 A typical biorthogonal basis function.

Figure 8 Example of a non-intuitive Fourier transform pair. The solid line shows the amplitude and the dashed line the phase. The “V” phase profile in frequency leads to a double-pulse structure in time.

Figure 9 The Wigner representation (a), the Husimi representation (b), and the von Neumann representation (c) of the pulse in Fig. 8. All three representations allow the visualization of the pulse in time and frequency simultaneously. For a color version of this figure, see the color plate section.

Figure 10 Transformation of a Gaussian pulse from frequency to the von Neumann representation and back without periodic boundary conditions. The error in the back-transformed signal is quite significant (blue vs. red curve in (c)). Panel (a) shows the amplitude of the von Neumann representation and panel (b) the phase. Adapted from Ref. [15]. For a color version of this figure, see the color plate section.

Figure 11 Transformation of a Gaussian pulse from frequency to the von Neumann representation and back with periodic boundary conditions. The back-transformed signal agrees with the original signal to the accuracy of the computer (blue vs. red curve in (c)). Panel (a) shows the amplitude of the von Neumann representation and panel (b) the phase. Adapted from Ref. [15]. For a color version of this figure, see the color plate section.

Figure 12 (a) Error in the seventh eigenvalue of the harmonic oscillator for a rectangular phase space grid as a function of the basis set size N. The pvN, pvb, and Fourier grid methods all give identical

results (solid), 14 orders of magnitude more accurate than the usual vN basis (dashed). (b) Kinetic energy spectrum using the vN basis(dashed) and using the FGH, pvN, and bvN basis (solid). (c). Error in the 24th eigenvalue of the Morse potential as one discards basis functions from a rectangular phase space lattice. The pvb (solid), pvN (dashed), and Fourier grid (dotted) behave completely differently. Removing even one basis function from the pvN introduces significant error, while more than two-thirds of the pvb basis functions can be removed without introducing any significant error. Adapted from Ref. [16].

Figure 13 (a) The triangle potential. (b) Comparison of the error in the highest eigenvalue of the Fourier (dashed) and pvb (solid) methods as a function of basis set size. Adapted from Ref. [16]. For a color version of this figure, see the color plate section.

Figure 14 (a) Phase space area spanned in the bvN method (magenta) and in the pvN (or FGH) method (full rectangle) for a 1D Morse oscillator Morse. (b) Efficiency ratio (defined as number of basis functions per converged eigenstates) of the bvN (solid) and FGH (dashed) methods for the 1D Morse oscillator as a function of h. (c) Efficiency ratio of the bvN (triangles) and FGH (circles) methods for the 2D triangle potential of Fig. 13 as a function of h. The solid triangle and circle are the efficiencies in the classical limit. Adapted from Ref. [16]. For a color version of this figure, see the color plate section.

Figure 15 (a) The periodic von Neumann method does not require identical, evenly spaced Gaussians. One may tile the phase space any way one likes as long as the rectangular tiles have area h. Then a

basis of Gaussians whose centers and aspect ratios are matched to the rectangles will be a complete and stable basis. This flexibility in the positions and widths of the Gaussians can improve the efficiency of the pvN method significantly, particularly for problems that have multiple length scales. (b) The error in E_3 for the Coulomb potential as a function of basis set size. FGH (dashed), pvb (circles), and wpvb (solid). Adapted from Ref. [17].

Figure 16 Schematic diagram of electron motion on the attosecond time scale. Left: Strong field ionization and recollision, leading to high harmonic generation. Right: Strong field manipulation of electronic motion in a diatomic molecule. For a color version of this figure, see the color plate section.

Figure 17 Vector potentials, $A_{\mathrm{NIR}}(t)$ and $A_{\mathrm{XUV}}(t)$, of the NIR and XUV laser pulses applied to the model 1D atom. For a color version of this figure, see the color plate section.

Figure 18 Snapshots of the wavepacket coefficients $\{|c_j|^2\}_{j\in\mathcal{A}}$ shown by ellipses located at the Gaussian centers $\{(q_j,p_j)\}_{j\in\mathcal{A}}$. The colors of the ellipses indicate the magnitude of $|c_j|^2$ according to the scale above the figure. The sequence of dark blue dots represent the simple-man trajectories (i.e., classical trajectories evolving in the presence of the field without the Coulomb potential) for direct ionization; the light blue dots represent the rescattered simple-man trajectories. The dark blue + marks represent the simple-man trajectories absorbing one XUV photon in the presence of the NIR field. The snapshots were taken at (a) $t = -2.06$, (b) $t = 0.69$, and (c) $t = 2.06$ in units of NIR cycles. These times are indicated by the

green × marks in Fig. 17. Adapted from Ref. [18]. For a color version of this figure, see the color plate section.

Figure 19 Comparison of the photoelectron momentum distributions obtained with the reduced pvb basis (blue solid line) and full pvb basis (red dashed line). The momentum distribution from a simulation without the XUV pulse (using the full pvb basis) is also shown (gray solid line). The vertical dashed lines indicate the cut-offs of the direct (N1 and N1′) and rescattered (N2 and N2′) photoelectrons, as well as the NIR-streaked single-XUV-photon ionization peaks (X1 and X1′), estimated by the simple-man model. Adapted from Ref. [18]. For a color version of this figure, see the color plate section.

Figure 20 The error ε as a function of $\langle N_{\mathcal{A}} \rangle / N$ (black × marks). The horizontal error bars indicate the range of $N_{\mathcal{A}}(t)/N$ in $t_{\min} \leq t \leq t_{\max}$. The data marked by the red filled circle is from the simulation shown in Figs. 18 and 19. Adapted from Ref. [18]. For a color version of this figure, see the color plate section.

Figure 21 The splat signal in time (a), frequency (b), and pgb (c) representations. Adapted from Ref. [19]. For a color version of this figure, see the color plate section.

Figure 22 The norm of the error of the reconstructed signal as a function of the number of basis functions using the DFT (red), the DGE with an additional correction due to Porat (green), the pgb (blue), and the pgb with a correction developed by Porat (black). Adapted from Ref. [19]. For a color version of this figure, see the color plate section.

dashed lines in the phase diagram in the temperature T–density $\rho\sigma^3$ representation in (d). The free-energy density $f = F/V$ versus the density $\rho\sigma^3$, showing (a) the existence of a symmetry-breaking liquid–solid transition at high temperature, (b) a symmetry-conserving gas–liquid transition at low densities and a symmetry-breaking liquid–solid transition at higher densities at intermediate temperature, (c) a metastable gas–liquid transition with respect to a stable liquid–solid transition at low temperature.

Figure 3 Phase diagram for a binary hard-sphere mixture with size ratio $q = 0.82$ in the reduced pressure p–composition x representation with $p = \beta P \sigma^3_L$, $x = N_S/(N_S + N_L)$, $N_{(S)L}$ the number of (small) large spheres, and $\sigma_{(S)L}$ the diameter of (small) large spheres. Adapted from Ref. [38]. “FCC(S)” denotes a face-centered cubic crystal of small spheres, “FCC(L)” denotes a face-centered cubic crystal of large spheres. The phase coexistence regions are labeled “FCC(L) + Laves,” “FCC(S) + Laves,” “Laves + Fluid,” etc.

Figure 4 Phase diagram for a binary hard-sphere mixture with size ratio $q = 0.3$ in the reduced pressure p–composition x_S representation with $p = \beta P \sigma^3_L$, $x_S = N_S/(N_S + N_L)$, $N_{(S)L}$ the number of (small) large spheres, and $\sigma_{(S)L}$ the diameter of (small) large spheres [131]. The interstitial solid solution is denoted by “ISS,” “FCC(S)” denotes a face-centered cubic crystal of small spheres, “FCC(L)” denotes a face-centered cubic crystal of large spheres, and “LS_6” denotes a binary superlattice structure. A typical configuration of the ISS phase is shown in the inset of the phase diagram. (a) shows a configuration

of the pure FCC of large spheres, (b) of the NaCl phase, and (c) the LS_6 phase. The top inset in the phase diagram shows that the filling fraction of the octahedral holes in the coexisting ISS phase increases with pressure from 0 (pure FCC of large spheres) to 1 (NaCl phase). The trajectory of a single small sphere in the FCC lattice of big spheres at a volume fraction $\eta_L = 0.6$. Note that the small particle in an octahedral hole (d) hops first to a tetrahedral hole (e), and then to the next octahedral hole (f). Adapted from Ref. [131].

Figure 5 The phase diagram of hard dumbbells in the reduced density ρ^* (and packing fraction ϕ) versus $L^* = L/\sigma$ representation, where L is the distance between the centers of the spheres and σ is the diameter of the spheres as denoted in the schematic picture of a dumbbell [56, 57, 167, 168]. Hence the model reduces to hard spheres for $L^* = 0$ and to tangent spheres for $L^* = 1$. The dimensionless density is defined as $\rho^* = d^3N/V$ with N the number of particles, V the volume, and $d^3/\sigma^3 = 1 + 3L^*/2 - 1/2(L^*)^3$ is the volume of a dumbbell divided by that of a sphere with diameter σ, so that d is the diameter of a sphere with the same volume as the dumbbell. "F" denotes the fluid phase and "CP1" the periodic crystal. The aperiodic phase "aper" is stable only in a narrow region of the phase diagram. The stable face-centered cubic type plastic crystal is denoted by filled squares, the hexagonal-close-packed plastic crystal phase is denoted by empty squares. Adapted from Ref. [57].

Figure 6 The phase diagram of hard snowman particles in the size ratio q–packing fraction η representation, with $q = \sigma_s/\sigma_l$ ranging from 0 (the

hard sphere) to $q = 1$ (the tangential dumbbell), σ_s is the diameter of the smaller sphere and σ_l is the diameter of the larger sphere. Adapted from Ref. [170]. The packing fraction is defined as $\eta = Nv_0/V$, where v_0 is the particle volume for a given q value. Circles indicate coexisting phases, while the lines are intended to guide the eye. At the top of the plot we indicate the density of closest packing, with triangles indicating the crossover from one close-packed structure to another. “Isotropic” denotes the isotropic fluid phase, “NaCl, CrB, γCuTi, αIrV, and FCC*” denotes aperiodic crystal structures, which are stabilized by the degeneracy of the crystal structure (i.e., the number of bond configurations). “Rotator” denotes a plastic crystal phase.

Figure 7 The phase diagram of hard asymmetric dumbbell particles with size ratio $q = \sigma_s/\sigma_l = 0.5$ in the reduced center-of-mass distance L^*–packing fraction η representation. Adapted from Ref. [171]. The diameter of the (smaller) larger sphere is denoted by (σ_s) σ_l and the reduced center-of-mass distance is defined as $L^* = (2L + \sigma_s - \sigma_l)/2\sigma_l$ ranging from 0 (hard spheres) to 0.5 (tangential snowman-shaped particles). “APC” denotes the aperiodic CrB phase, “CrB” denotes the periodic CrB crystal, “NaCl” denotes the periodic NaCl crystal phase. Circles indicate coexisting phases, while the lines are guides to the eye. The density of the maximum packing is denoted by the line at the top of the figure, and the triangles indicate crossover points from one close-packed structure to another.

Figure 8 (a) Side view of an oblate spherocylinder for $L/\sigma = 0.2$, where L denotes the thickness of the plate and σ the diameter. An oblate spherocylinder is

obtained by padding a disk of diameter D, as indicated by the black line, with a layer of uniform thickness $L/2$. (b) The phase diagram of hard oblate spherocylinders in the packing fraction ϕ–reduced thickness L/σ representation. The state points in the dark grey area are inaccessible since they lie above the maximum close packing line. "X_{aligned}" and "X_{tilted}" denote the aligned and tilted crystal structures as shown in (c) and (d), "iso" denotes the isotropic fluid, "nem" the nematic phase, and "col" the columnar phase. The solid lines are a guide to the eye, connecting coexistence points. The data for $L/\sigma = 0$ are taken from Ref. [182]. (c) The unit cell of the tilted crystal phase for $L/\sigma = 0.3$ and (d) the aligned crystal phase for $L/\sigma = 0.5$. Adapted from Ref. [53].

Figure 9 (a) The bulk phase diagram of hard cubes as a function of packing fraction η. A stable fluid phase is found for $\eta < 0.45$, and a stable simple cubic crystal phase with vacancies is observed for $\eta > 0.50$. Coexistence between the crystal and fluid is found for $0.45 < \eta < 0.50$. (b) A typical configuration of a simple cubic crystal phase of hard cubes at $\eta = 0.52$ and vacancy concentration of 1.6%. The particles surrounding the delocalized defects are yellow. The defect at the top has six cubes sharing seven lattice positions, the defect at the right bottom has three cubes sharing four lattice positions, and the defect at the left bottom shows seven cubes spread over eight lattice positions. Adapted from Ref. [54].

Figure 10 (a) The shape of superballs interpolates between octahedra ($q = 0.5$) and cubes ($q = \infty$) via spheres ($q = 1$). (b) The bulk phase diagram of hard superballs as a function of packing fraction ϕ versus $1/q$ (bottom axis) and q (top axis) representation

where q is the shape parameter [82]. The "C_1" and "C_0" crystal phases are defined in Refs. [50, 51], where the particles of the same color are in the same layer of stacking. The solid diamonds indicate close packing, and the locations of triple points are determined by extrapolation as shown by the dashed lines. The phase boundaries for hard cubes are taken from Ref. [54]. Adapted from Ref. [82].

Figure 11 Phase diagram of hard bowl-shaped particles in the packing fraction (ϕ) versus thickness (D/σ) representation. Adapted from Refs. [90, 91]. The light grey areas denote the coexistence regions, while the dark grey area indicates the forbidden region as it exceeds the maximum packing fraction of the bowls. The lines are a guide to the eye. The inset in the phase diagram shows the theoretical model of the bowl-shaped particle, which is the solid of revolution of a crescent around the axis as indicated by the dashed line. The thickness of the bowl is denoted by D and the diameter of the bowl by σ. The stable crystal phases, IX, IX′, IB, and fcc[2], the "fluid," and hexagonal columnar phase "col" are drawn schematically below the phase diagram.

Chapter 3

Figure 1 Representatives of unusual clusters: (a) B_9^- is a wheel [1]. (b) TaB_{10}^- [2]. (c) Au_{20} [3]. (d) Clusters containing tetracoordinated planar C and Si atoms [4]. (e) Stannaspherene [5].

Figure 2 (a) Left: $LiAl_4^-$ structure; right: atomic charges, and populated valence MOs of Al_4^{2-} [43]. (b) Left: $Li_3Al_4^-$ structure and atomic charges; right: populated valence MOs of Al_4^{4-} [41]. MO types are

labeled as σ-radial, σ-peripheral, π-, or LP (lone pair), as described in the text.

Figure 3 Boron wheels, and their delocalized valence MOs responsible for the doubly aromatic character of chemical bonding [1]. For a color version of this figure, see the color plate section.

Figure 4 $Ta_3O_3^-$ the first cluster possesses π- and δ-aromaticity [45]. Reproduced with permission from JWS, Angewandte Chemie International Edition, April 30 2007.

Figure 5 Structures of the gold clusters derived from the tetrahedral Au_{20} species and patterns of chemical bonding according to AdNDP [3]. Reproduced with permission from American Chemical Society, The Journal of Physical Chemistry A, Feb 2009. For a color version of this figure, see the color plate section.

Figure 6 B_6^{2-} and its valence MOs. The decomposition of the MOs onto those of π- and σ-type, and localizable as 2c–2e B–B bonds is shown [51].

Figure 7 B_6^{2-} and Al_6^{2-} have different structures rooted in the differences in chemical bonding [50, 56, 57]. The B cluster has covalent bonding that defines its planar shape, whereas in the Al cluster all bonding is delocalized. Reproduced with permission from American Chemical Society, The Journal of Physical Chemistry Letters, August 2011.

Figure 8 $LiNa_4^-$ versus LiK_4^-: their different global minimum structures and valence MOs. The s–p hybridization of AOs on Li in one case but not in the other is illustrated [6].